Metodología para evaluar el desempeño en economía circular en el reciclaje de PET en Cuba / (Methodology for evaluating performance in the circular economy in PET recycling in

Original
Metodología para evaluar el desempeño en economía circular en el reciclaje de PET en Cuba / (Methodology for evaluating performance in the circular economy in PET recycling in Cuba) / Gutiérrez Benítez, Omar; Mckenn Tavio, Lesyán; Jiménez Borges, Reinier; Castro Rodriguez, David Javier. - In: UNIVERSIDAD Y SOCIEDAD. - ISSN 2218-3620. - ELETTRONICO. - 17:6(2025), pp. 1-9.

Publisher:
Editorial "Universo Sur"

Published
DOI:

NASA/TP–2011-217315

Dynamic Shape Reconstruction of Three-Dimensional Frame Structures Using the Inverse Finite Element Method

Marco Gherlone, Priscilla Cerracchio, Massimiliano Mattone, and Marco Di Sciuva
Department of Aeronautics and Space Engineering
Politecnico di Torino, Torino, Italy

Alexander Tessler
Langley Research Center, Hampton, Virginia

December 2011

NASA STI Program . . . in Profile

Since its founding, NASA has been dedicated to the advancement of aeronautics and space science. The NASA scientific and technical information (STI) program plays a key part in helping NASA maintain this important role.

The NASA STI program operates under the auspices of the Agency Chief Information Officer. It collects, organizes, provides for archiving, and disseminates NASA's STI. The NASA STI program provides access to the NASA Aeronautics and Space Database and its public interface, the NASA Technical Report Server, thus providing one of the largest collections of aeronautical and space science STI in the world. Results are published in both non-NASA channels and by NASA in the NASA STI Report Series, which includes the following report types:

- TECHNICAL PUBLICATION. Reports of completed research or a major significant phase of research that present the results of NASA programs and include extensive data or theoretical analysis. Includes compilations of significant scientific and technical data and information deemed to be of continuing reference value. NASA counterpart of peer-reviewed formal professional papers, but having less stringent limitations on manuscript length and extent of graphic presentations.

- TECHNICAL MEMORANDUM. Scientific and technical findings that are preliminary or of specialized interest, e.g., quick release reports, working papers, and bibliographies that contain minimal annotation. Does not contain extensive analysis.

- CONTRACTOR REPORT. Scientific and technical findings by NASA-sponsored contractors and grantees.

- CONFERENCE PUBLICATION. Collected papers from scientific and technical conferences, symposia, seminars, or other meetings sponsored or co-sponsored by NASA.

- SPECIAL PUBLICATION. Scientific, technical, or historical information from NASA programs, projects, and missions, often concerned with subjects having substantial public interest.

- TECHNICAL TRANSLATION. English-language translations of foreign scientific and technical material pertinent to NASA's mission.

Specialized services also include creating custom thesauri, building customized databases, and organizing and publishing research results.

For more information about the NASA STI program, see the following:

- Access the NASA STI program home page at *http://www.sti.nasa.gov*

- E-mail your question via the Internet to help@sti.nasa.gov

- Fax your question to the NASA STI Help Desk at 443-757-5803

- Phone the NASA STI Help Desk at 443-757-5802

- Write to:
  NASA STI Help Desk
  NASA Center for AeroSpace Information
  7115 Standard Drive
  Hanover, MD 21076-1320

NASA/TP–2011-217315

Dynamic Shape Reconstruction of Three-Dimensional Frame Structures Using the Inverse Finite Element Method

Marco Gherlone, Priscilla Cerracchio, Massimiliano Mattone, and Marco Di Sciuva
Department of Aeronautics and Space Engineering
Politecnico di Torino, Torino, Italy

Alexander Tessler
Langley Research Center, Hampton, Virginia

National Aeronautics and
Space Administration

Langley Research Center
Hampton, Virginia 23681-2199

December 2011

Available from:

NASA Center for AeroSpace Information
7115 Standard Drive
Hanover, MD 21076-1320
443-757-5802

Abstract

A robust and efficient computational method for reconstructing the three-dimensional displacement field of truss, beam, and frame structures, using measured surface-strain data, is presented. Known as "shape sensing", this inverse problem has important implications for real-time actuation and control of smart structures, and for monitoring of structural integrity. The present formulation, based on the inverse Finite Element Method (iFEM), uses a least-squares variational principle involving strain measures of Timoshenko theory for stretching, torsion, bending, and transverse shear. Two inverse-frame finite elements are derived using interdependent interpolations whose interior degrees-of-freedom are condensed out at the element level. In addition, relationships between the order of kinematic-element interpolations and the number of required strain gauges are established. As an example problem, a thin-walled, circular cross-section cantilevered beam subjected to harmonic excitations in the presence of structural damping is modeled using iFEM; where, to simulate strain-gauge values and to provide reference displacements, a high-fidelity MSC/NASTRAN shell finite element model is used. Examples of low and high-frequency dynamic motion are analyzed and the solution accuracy examined with respect to various levels of discretization and the number of strain gauges.

Nomenclature

(x, y, z)	Cartesian coordinate system
(θ, x, r)	cylindrical coordinate system
(x_1^*, x_2^*, x_3^*)	local "strain-gauge" coordinate system
E, G, ν, ρ	Young's modulus, shear modulus, Poisson ratio, and density
L, A	length and cross-sectional area of frame member
I_y, I_z	area moments of inertia with respect to the y- and z-axis
I_P	polar moment of inertia
u_x, u_y, u_z	displacements along x-, y-, and z-axis

u , v , w	displacements along along x -, y -, and z -axis
θ_x, θ_y, θ_z	rotations about x -, y -, and z -axis
$\mathbf{u} \equiv \left[u, \quad v, \quad w, \quad \theta_x, \quad \theta_y, \quad \theta_z\right]^T$	vector of the kinematic variables
$\mathbf{u}^h$	vector of the approximated kinematic variables
ε_x , γ_{xz} , γ_{xy}	non vanishing components of the strain tensor for the Timoshenko beam theory in the (x,y,z) coordinate system
ε_x , ε_θ , $\gamma_{x\theta}$	components of the strain tensor for the Timoshenko beam theory in the (θ, x) plane
ε_2^*	strain measured by the strain-gauge
σ_x , σ_θ , $\tau_{x\theta}$	components of the stress tensor for the Timoshenko beam theory in the (θ, x) plane
$e_i \quad (i = 1, \ldots, 6)$	section strains
$\mathbf{e} \equiv [e_1, \quad e_2, \quad e_3, \quad e_4, \quad e_5, \quad e_6]^T$	vector of the section strains
$\mathbf{e}^\varepsilon$	experimentally evaluated section strains
N, Q_y, Q_z, M_x, M_y, M_z	section forces and moments
A_x, G_y, G_z, J_x, D_y, D_z	axial rigidity, shear rigidities, torsional rigidity and bending rigidities of the beam
k_y^2 , k_z^2	shear correction factors
q_x, q_y, q_z	distributed loads along the x-, y-, and z-direction
Φ	least-squares functional
$\mathbf{u}^e$	vector of the nodal degrees of freedom of the inverse finite element
$\mathbf{N}$	matrix of the shape functions relating the kinematic variables to the nodal degrees of freedom
$\mathbf{B}$	matrix of the shape functions relating the section strains to the nodal degrees of freedom
w_k^0, $w_k \quad (k = 1, \ldots, 6)$	weighting coefficients
L^e, A^e, I_y^e, I_z^e, I_P^e	length, cross-sectional area and moments of inertia of frame inverse element
n , x_i	number and axial coordinate of the locations where the section strains are evaluated

$\mathbf{k}^{\mathbf{e}}$, $\mathbf{f}^{\mathbf{e}}$	matrix and vector of the single inverse element governing equation
$\mathbf{K}$, $\mathbf{F}$	matrix and vector of the whole structure governing equation
$L_i^{(1)}(\xi)$	linear Lagrange polynomials
$L_j^{(2)}(\xi)$	quadratic Lagrange polynomials
$N_j^{(3)}(\xi), \overline{N}_k^{(3)}(\xi)$	special cubic polynomials
$L_k^{(4)}(\xi)$	quartic Lagrange polynomials
β	orientation of a strain-gauge with respect to the beam axis
R_{ext}	external radius of the circular cross-sectio
R, t	radius and thickness of the thin-walled circular cross section
F_z(t)	time varying applied force
F_{z0}	amplitude of the applied force
f_0	frequency of the applied force

1 Introduction

Real-time reconstruction of structural deformations using measured strain data, is a key technology for actuation and control of smart structures, as well as for Structural Health Monitoring (SHM) [1]. Known as "shape sensing", this inverse problem is commonly formulated with the assumption that multiple strain sensors at various structural locations provide real-time strain measurements. Most inverse algorithms use some type of Tikhonov's regularization, which is manifested by constraint (regularity) terms that ensure a certain degree of solution smoothness (refer to [2-5] and references therein).

Most of the shape sensing efforts focused exclusively on beam-bending problems. Davis et al. [6] used optimized trial functions and weights to reconstruct a simple static-beam response from discrete strain measurements. To model more complex deformations, the approach requires a large number of trial functions and strain sensors. Kang et al. [7] used vibration mode shapes to reconstruct a beam response due to dynamic excitation. In their approach, modal coordinates are computed using strain-displacement relationships and measured surface strains; the method requires the same number of mode shapes and strain sensors. Kim et al. [8] and Ko et al. [9] used classical beam equations to integrate discretely measured strains to determine the deflection of a beam. By regression of experimental strain data and by accounting for the applied loading, Kim et al. [8] obtained a continuous curvature function, leading to the evaluation of beam deflection. Ko et al. [9] developed a load-independent method by approximating the beam curvature using piece-wise continuous polynomials; the authors demonstrated the validity of a one-dimensional scheme by evaluating the deflection and cross-section twist of an aircraft wing.

To enable shape-sensing analyses of plates undergoing bending deformations, Bogert et al. [10] examined a modal transformation method that allows the development of suitable strain-displacement transformations. The approach makes use of a large number of natural vibration modes. When applied to high-fidelity finite element models, however, the method requires a computationally intensive eigenvalue analysis and a detailed description of the elastic and inertial material properties. Jones et al. [11] employed a least-squares formulation for shape sensing of a cantilever plate, where the axial strain was fitted with a cubic polynomial. The strain field was then integrated with the use of approximate boundary conditions at the clamped end to obtain plate deflections according to classical bending assumptions. Shkarayev et al. [12,13] used a two-step solution procedure: the first step involves the structural analysis of a plate/shell finite element model, and the second, a least-squares algorithm. The methodology reconstructs the applied loading first, which then leads to the displacements. In a series of four papers, Mainçon and co-authors [14-17] developed a finite element formulation that seeks the solution for the displacements and loads simultaneously, requiring a priori knowledge of a subset of applied loading and the material properties. The solution procedure minimizes a cost function consisting of unknown loads and differences between the measured and estimated quantities (displacements or strains); the cost function is regularized by way of equilibrium constraints. The number of unknowns is three times the number of the degrees-of-freedom in the finite element discretization. Importantly, the accuracy of the solution strongly depends on the choice of suitable weights; these are computed from a complex procedure involving the probability distributions of the unknown loads and measured data. In [16,17], sensitivity analyses were carried out for truss structures, investigating variations in the input data as well as the modeling errors. Nishio et al. [18] employed a weighted-least-squares formulation to reconstruct, on the basis of measured strain data, the deflection of a composite cantilevered plate. The weighting coefficients in the least-square terms were adjusted in order to account for the inherent errors in the measured strain data. The weights were computed for a given data-acquisition apparatus, load case, and test article, with the consequent difficulties in generalizing the procedure.

Many of the aforementioned inverse methods either lack generality with respect to structural topology and boundary conditions, or require sufficiently accurate loading and/or elastic-inertial material information – the kind of data that are either unavailable or difficult to obtain outside the laboratory environment; for these reasons, such approaches are generally unsuited for use in onboard SHM algorithms. A well-suited algorithm for SHM should be: (1) general enough to accommodate complex structural topologies and boundary conditions (e.g., built-up aircraft structures), (2) robust, stable, and accurate under a wide range of loadings, material systems, inertial/damping characteristics, and inherent errors in the strain measurements, and (3) sufficiently fast for real-time applications.

An algorithm that appears to fulfill the aforementioned requirements was recently developed by Tessler and Spangler [1,19]. The methodology, labeled the inverse Finite Element Method (iFEM), employs a weighted-least-square variational principle which is discretized by C0-continuous finite elements that accommodate arbitrarily positioned and oriented strain-sensor data. The iFEM framework, providing accurate and stable solutions of the displacement and strain fields for a discretized structural domain, is amenable to any type of structural modeling including frame (truss and beam), plate, shell, and solid idealizations. Because only strain-displacement relations are used in the formulation, both static and dynamic response can be reconstructed without any a priori knowledge of material, inertial, loading, or damping structural properties. To model arbitrary plate and shell structures, Tessler [20] developed, using first-order shear-deformation theory, a three-node inverse shell element. Numerically generated [20] and experimentally measured-strain data [21,22] were used to assess robustness and accuracy of the formulation.

The present paper consolidates the authors' recent efforts [23-24] and presents the development and assessment of simple and efficient inverse-frame finite elements. The methodology permits effective and computationally efficient shape-sensing analyses to be performed on truss, beam, and frame structures instrumented with strain gauges. The kinematic assumptions are those of Timoshenko shear-deformation theory [25]; they incorporate stretching, torsion, bending, and transverse shear deformation modes in three dimensions. The formulation uses a least-squares variational principle that is specialized from [19] for three-dimensional frame analysis. The variational framework, in conjunction with suitable finite element discretizations involving inverse finite elements, yields a system of linear algebraic equations; the equations are efficiently solved for the unknown displacement degrees-of-freedom (dof's), thus providing the deformed structural-shape predictions.

In the remainder of the paper, the kinematic assumptions for a three-dimensional frame are discussed, followed by the description of the least-squares variational principle suitable for three-dimensional deformations of frame structures. This is followed by a discussion of two C^0-continuous, inverse-frame elements that use the well-established interdependent interpolations that resolve the shear locking effect. Finally, to examine the predictive capabilities of the inverse elements for a given set of distributed strain gauges, shape-sensing studies are carried out for a cantilevered beam undergoing harmonic excitations in the presence of structural damping.

2 Governing equations

Consider a straight frame member of constant cross-section referred to the three-dimensional Cartesian coordinates (x,y,z) as depicted in Figure 1; the coordinate origin, O, is located at the cross-section's center of mass, which is also coincident with the shear center. The longitudinal, elastic x-axis is normal to the cross-sectional plane (y, z), where y and z are the cross-section's principal inertial axes. The frame member has length L and its cross-section has area A, area moments of inertia with respect to the y- and z-axis I_y and I_z, respectively, and polar moment of inertia $I_P = I_y + I_z$ (Figure 1). The frame member is made of an isotropic homogeneous material, represented by the elastic constants: E (Young's modulus), G (shear modulus), and v (Poisson ratio).

The three Cartesian components of the displacement vector that are consistent with the kinematic assumptions of Timoshenko theory [25] for three-dimensional deformations are given by

$$
\begin{aligned}
u_x(x,y,z) &= u(x) + z\theta_y(x) - y\theta_z(x) \\
u_y(x,y,z) &= v(x) - z\theta_x(x) \\
u_z(x,y,z) &= w(x) + y\theta_x(x)
\end{aligned}
\tag{1}
$$

where u_x, u_y, and u_z are the displacements along the x, y, and z axes, respectively, with u, v, and w denoting the displacements at $y = z = 0$; θ_x, θ_y, and θ_z are the rotations about the three coordinate axes; positive orientations for the displacements and rotations are depicted in Figure 1. These kinematic assumptions neglect the effect of axial warping due to torsion, i.e., each cross-section remains flat and rigid with respect to thickness-stretch deformations along the y and z axes. The six kinematic variables can be grouped in vector form as

$$
\mathbf{u} \equiv \left\{ u, \quad v, \quad w, \quad \theta_x, \quad \theta_y, \quad \theta_z \right\}^T \tag{2}
$$

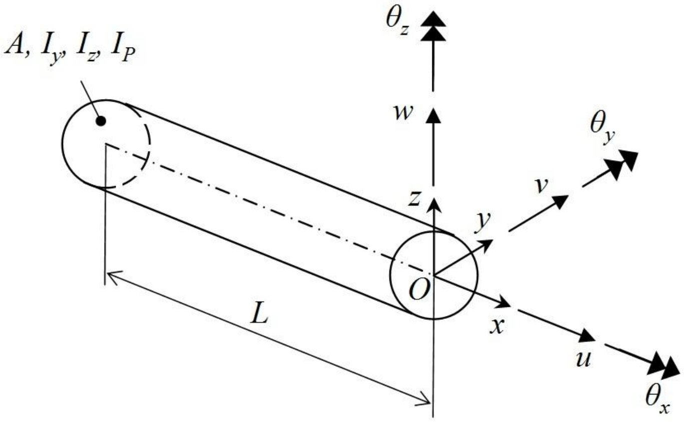

Figure 1: Beam geometry and kinematic variables.

Adhering to the small-strain hypothesis, the non-vanishing strain components have the form

$$
\begin{aligned}
\varepsilon_x(x,y,z) &= e_1(x) + z\,e_2(x) + y\,e_3(x) \\
\gamma_{xz}(x,y) &= e_4(x) + y\,e_6(x) \\
\gamma_{xy}(x,z) &= e_5(x) - z\,e_6(x)
\end{aligned}
\tag{3}
$$

where

$$\mathbf{e(u)} \equiv \{e_1, \quad e_2, \quad e_3, \quad e_4, \quad e_5, \quad e_6\}^T \tag{4}$$

denote the section strains of the theory, given by

$$\begin{array}{ll} e_1(x) \equiv u_{,x}(x) & e_4(x) \equiv w_{,x}(x) + \theta_y(x) \\ e_2(x) \equiv \theta_{y,x}(x) & e_5(x) \equiv v_{,x}(x) - \theta_z(x) \\ e_3(x) \equiv -\theta_{z,x}(x) & e_6(x) \equiv \theta_{x,x}(x) \end{array} \tag{5}$$

The section forces (*N*, Q_y, and Q_z) and moments (M_x, M_y, and M_z) are related to the section strains, e_i, by way of the constitutive equations (refer to Figure 2)

$$\begin{array}{ll} \mathrm{N} = A_x e_1 & \mathrm{M}_x = J_x e_6 \\ \mathrm{Q}_y = G_y e_5 & \mathrm{M}_y = D_y e_2 \\ \mathrm{Q}_z = G_z e_4 & \mathrm{M}_z = D_z e_3 \end{array} \tag{6}$$

where $A_x \equiv EA$ is the axial rigidity; $G_y \equiv k_y^2 GA$ and $G_z \equiv k_z^2 GA$ are the shear rigidities, with k_y^2 and k_z^2 denoting the shear correction factors; $J_x \equiv GI_P$ is the torsional rigidity and $D_y \equiv EI_y$ and $D_z \equiv EI_z$ denote the bending rigidities.

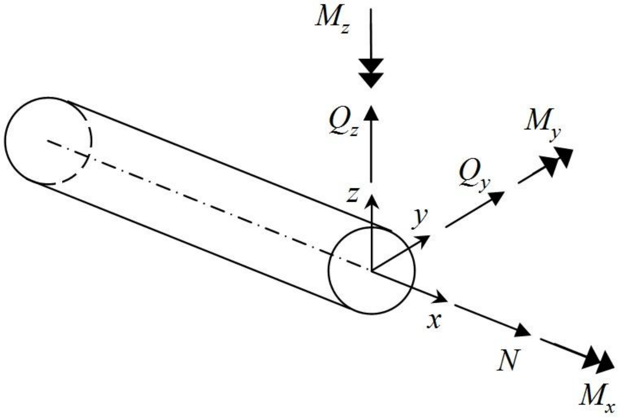

Figure 2: Beam section forces and moments.

The equilibrium equations that correspond to the distributed loads $q_x(x)$, $q_y(x)$, and $q_z(x)$ along the *x*, *y* and *z* directions, are

$$\begin{aligned} \frac{\mathrm{dN}}{\mathrm{d}x} &= -q_x & \frac{\mathrm{dM}_x}{\mathrm{d}x} &= 0 \\ \frac{\mathrm{dQ}_y}{\mathrm{d}x} &= -q_y & \frac{\mathrm{dM}_y}{\mathrm{d}x} &= \mathrm{Q}_z \\ \frac{\mathrm{dQ}_z}{\mathrm{d}x} &= -q_z & \frac{\mathrm{dM}_z}{\mathrm{d}x} &= \mathrm{Q}_y \end{aligned} \tag{7}$$

To reconstruct the deformed shape of a frame-member for which certain in-situ strain measurements are known, a functional $\Phi(\mathbf{u})$ that matches in a least-squares sense the complete set of analytic section strains, $\mathbf{e}(\mathbf{u})$, to the in-situ section strains, $\mathbf{e}^{\varepsilon}$, is minimized with respect to the kinematic variables, $\mathbf{u}$; $\Phi(\mathbf{u})$ functional can be written as

$$\Phi(\mathbf{u}) = \left\| \mathbf{e}(\mathbf{u}) - \mathbf{e}^{\varepsilon} \right\|^2 \tag{8}$$

This functional may be used in a finite element framework by introducing a discretization in which the element kinematic field is interpolated by C^0-continuous shape functions,

$$\mathbf{u}(x) \simeq \mathbf{u}^h = \mathbf{N}(x)\mathbf{u}^e \tag{9}$$

where $\mathbf{N}(x)$ denotes the shape functions and $\mathbf{u}^e$ nodal dof's. Thus, the total least-squares functional is a sum of the individual element contributions, $\Phi^e(\mathbf{u}^h)$, i.e., $\Phi = \sum_{e=1}^{N} \Phi^e$, with *N* denoting the total number of elements. Accounting for the axial stretching, bending, twisting, and transverse shearing, the element functional is given by the dot product of the weighting coefficient vector, $\mathbf{w} \equiv \{w_k\} = \{w_1^0,\ \ w_2^0\left(I_y^e / A^e\right),\ \ w_3^0\left(I_z^e / A^e\right),\ \ w_4^0,\ \ w_5^0,\ \ w_6^0\left(I_P^e / A^e\right)\}$, and the least-squares component vector, $\mathbf{\Phi} \equiv \{\Phi_k^e\}$,

$$\Phi^e(\mathbf{u}^h) \equiv \mathbf{w} \cdot \mathbf{\Phi} \tag{10}$$

where $w_k^0 \quad (k = 1, \ldots, 6)$ denote dimensionless weighting coefficients; A^e, I_y^e, I_z^e, and I_P^e are, respectively, the cross-section area, moments of inertia with respect to the y- and z-axis, and polar moment of inertia of the element, and

$$\Phi_k^e \equiv \frac{L^e}{n} \sum_{i=1}^{n} \left[e_k\left(x_i\right) - e_k^{\varepsilon i} \right]^2 \quad (k = 1, \ldots, 6) \tag{11}$$

denote the least-squares components of the element functional, where L^e denotes the element length; n and x_i ($0 \le x_i \le L^e$) are, respectively, the number and the axial coordinate of the locations where the section strains are evaluated, and the superscript εi is used to denote the section strains that are computed from the strain-sensor values (experimental values) at the location x_i. The w_k^0 coefficients may be assigned different values to enforce a stronger or weaker correlation between the measured section-strain components and their analytic counterparts, i.e., a larger value of w_k^0 enforces a stronger correlation, whereas a smaller value enforces a weaker correlation.

Substituting Eq. (9) into Eq. (3) gives the section strains in terms of the nodal dof's as

$$e_k = \mathbf{B}_k \mathbf{u}^e \quad (k = 1, \ldots, 6) \tag{12}$$

A vector form of Eq. (12) that incorporates all six section strains is given by

$$\mathbf{e}(\mathbf{u}) = \mathbf{B}(x)\mathbf{u}^e \tag{13}$$

where the matrix $\mathbf{B}(x)$ contains the derivatives of the shape functions $\mathbf{N}(x)$ ($\mathbf{B}(x)$ is defined in Appendix B for the case of shape functions presented in Sec. 3.) Substituting Eq. (13) into Eq. (11) and then Eq. (10) results in the following quadratic form

$$\Phi^e = \frac{1}{2}\left(\mathbf{u}^e\right)^T \mathbf{k}^e \mathbf{u}^e - \left(\mathbf{u}^e\right)^T \mathbf{f}^e + \mathbf{c}^e \tag{14}$$

where $\mathbf{c}^e$ is a constant while $\mathbf{k}^e$ and $\mathbf{f}^e$ are defined as follows

$$\mathbf{k}^{\mathbf{e}} = \sum_{k=1}^{6} w_k \mathbf{k}_k^{\mathbf{e}}, \quad \mathbf{f}^{\mathbf{e}} = \sum_{k=1}^{6} w_k \mathbf{f}_k^{\mathbf{e}} \tag{15}$$

with

$$\mathbf{k}_k^{\mathbf{e}} \equiv \frac{L^e}{n}\sum_{i=1}^{n}\left[\mathbf{B}_k^T\left(x_i\right)\mathbf{B}_k\left(x_i\right)\right],\quad \mathbf{f}_k^{\mathbf{e}} \equiv \frac{L^e}{n}\sum_{i=1}^{n}\left[\mathbf{B}_k^T\left(x_i\right)e_k^{\varepsilon i}\right] \qquad (k=1,...,6) \tag{16}$$

Note that $\mathbf{k}^e$ resembles an element stiffness matrix of the direct finite element method and $\mathbf{f}^e$ resembles the load vector; $\mathbf{k}^e$ is a function of the measurement locations, x_i, whereas $\mathbf{f}^e$ possesses the measured strain values. Minimization of functional Φ^e (see Eq. (14)) with respect to $\mathbf{u}^e$ leads to the inverse element matrix equation

$$\mathbf{k}^e\mathbf{u}^e = \mathbf{f}^e \tag{17}$$

The assembly of the finite element contributions, while accounting for the appropriate coordinate transformations and by specifying problem-dependent displacement boundary conditions, results in a non singular system of algebraic equations of the form

$$\mathbf{KU} = \mathbf{F} \tag{18}$$

The solution of these equations for the unknown dof's is efficient: the **K** matrix is inverted only once, since it is independent of the values of the measured strains. The **F** vector, however, is dependent on the measured strain values that change during deformation. Thus, at any strain-measurement update during deformation, the matrix-vector multiplication provides the solution for the unknown nodal displacement dof's, $\mathbf{U} = \mathbf{K}^{-1}\,\mathbf{F}$, where $\mathbf{K}^{-1}$ remains unchanged for a given distribution of strain sensors.

The remaining part of the element formulation involves the selection of suitable shape functions, symbolically defined by Eq. (9), and the computation of the experimental section strains, $e_k^{\varepsilon i}$, appearing in Eqs. (12),(13). In Sec. 3, the shape functions for two alternative inverse-frame elements, each having two nodes and twelve dof's, are derived. In Sec. 4, a procedure for computing $e_k^{\varepsilon i}$ is described; it relates the number of strain gauges to the interpolation order of the shape functions.

3 Element shape functions

In this section, inverse frame elements of 0th- and 1st-order are formulated. The elements use C^0-continuous interdependent interpolations that enable excellent predictions even for very slender frame members, without incurring any form of excessive stiffening due to shear locking [26]. The 0th-order shape functions are guided by Timoshenko equilibrium equations, Eqs. (7), that correspond to the forces and moments applied exclusively at the end nodes, resulting in constant distributions of the transverse-shear section strains. The 1st-order shape functions accommodate Eqs. (7) for uniformly distributed transverse loads, giving rise to linear distributions of the transverse-shear section strains.

A frame element is referred to a local axial coordinate $x \in \left[0, L^e\right]$, where L^e denotes the element length. Furthermore, a non-dimensional coordinate $\xi \equiv (2x/L^e - 1) \in \left[-1,1\right]$ is used to define the element shape functions (Figure 3). The initial nodal configurations are defined by the two end nodes, 1 (at $\xi = -1$) and 2 (at $\xi = +1$) and one or three interior nodes. Thus, the initial configuration for the 0th-order element has the interior node, *r* (at the midspan, $\xi = 0$); whereas the interior nodes of the 1st-order element are q (at $\xi = -1/2$), *r* (at $\xi = 0$), and *s* (at $\xi = +1/2$).

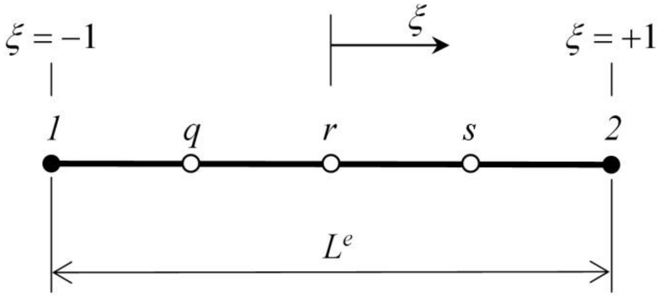

Figure 3: Inverse finite element geometry and nodal topology.

The initial nodal configurations of the 0th- and 1st-order elements are readily reduced to two nodes and twelve dof's by condensing out the interior dof's at the element level in a manner analogous to static condensation. The resulting elements have three-displacement and three-rotation dof's at each end node (Figure 4); thus, the dof's vector of the elements is

$$\mathbf{u}^e \equiv \left\{ u_1,\ v_1,\ w_1,\ \theta_{x1},\ \theta_{y1},\ \theta_{z1},\ u_2,\ v_2,\ w_2,\ \theta_{x2},\ \theta_{y2},\ \theta_{z2} \right\}^T \tag{19}$$

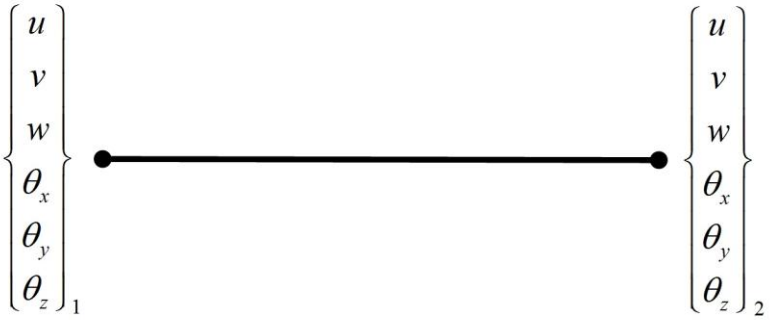

Figure 4: Two-node inverse finite element.

The process of condensing out the interior dof's results in the reduced element equations, $\mathbf{k}_R^e \mathbf{u}_R^e = \mathbf{f}_R^e$, where $\mathbf{k}_R^e$ is a function of the partitioned parts of the original $\mathbf{k}^e$ matrix, and $\mathbf{u}_R^e$ contains the end-node dof's. Since the unreduced $\mathbf{k}^e$ matrix is independent of the strain values, so is the $\mathbf{k}_R^e$ matrix. This implies that even for the elements with the condensed-out interior dof's, the corresponding system matrix, $\mathbf{K}$, is strain-value independent (refer to Eq. (18).)

3.1 0th-order element

The formulation of the 0th-order element is guided by Eqs. (7) for the loading case of end-node forces and moments. For this case, the axial force, twisting moment, and shear forces are constant along the element; whereas the bending moments are linear. Eqs. (7) in terms of the section strains (after Eqs. (6) have been introduced) indicate that the section strains e_i (i=1,4-6) are constant, and e_i (i=2,3) are linear. From Eqs. (5), it is deduced that u and θ_x are linear, θ_y and θ_z are parabolic, and v and w are cubic.

The inter-relationship of the polynomial order of the deflection variables, v and w, and bending rotations, θ_y and θ_z, can also be inferred from the definitions of the transverse shear section strains [24]

$$e_4 = \left(w_{,x} + \theta_y\right), \quad e_5 = \left(v_{,x} - \theta_z\right) \tag{20}$$

It is understood that in e_4 both $w_{,x}$ and θ_y should be represented by the same polynomial order and, similarly, in e_5 both $v_{,x}$ and θ_z should also have matching polynomial orders. The above interpolations give rise to quadratic interpolations for e_4 and e_5; they permit a consistent reduction of interior dof's for v and w by requiring a constant variation of these section strains across the element span

$$e_4 = const., \quad e_5 = const. \tag{21}$$

The complete set of interpolations for this element is thus given by

$$\begin{aligned}
&u(\xi) = \sum_{i=1,2} L_i^{(1)}(\xi) u_i, && \theta_x(\xi) = \sum_{i=1,2} L_i^{(1)}(\xi)\theta_{xi} \\
&\theta_y(\xi) = \sum_{j=1,r,2} L_j^{(2)}(\xi)\theta_{yj}, && \theta_z(\xi) = \sum_{j=1,r,2} L_j^{(2)}(\xi)\theta_{zj} \\
&v(\xi) = \sum_{i=1,2} L_i^{(1)}(\xi) v_i - \sum_{j=1,r,2} N_j^{(3)}(\xi)\theta_{zj}, && w(\xi) = \sum_{i=1,2} L_i^{(1)}(\xi) w_i + \sum_{j=1,r,2} N_j^{(3)}(\xi)\theta_{yj}
\end{aligned} \tag{22}$$

where $L_i^{(1)}(\xi)$ $(i=1,2)$ and $L_j^{(2)}(\xi)$ $(j=1,r,2)$ are, respectively, linear and quadratic Lagrange polynomials, and $N_j^{(3)}(\xi)$ $(j=1,r,2)$ are special-form cubic polynomials (refer to Appendix A.) Static condensation can be used to condense out the two interior dof's (θ_{yr} and θ_{zr}, refer to Eqs. (22)), thus, achieving a two-node element with twelve dof's (Figure 4, Eq. (19)).

3.2 1st-order element

Consider a frame element loaded by uniformly distributed transverse loads, $q_y(x)$ and $q_z(x)$. From Eqs. (7), after the substitution of Eqs. (6), it is readily deduced that e_4 and e_5 need to be linear and e_2 and e_3 parabolic. The u and θ_x variables remain linear as in Eq. (22). Moreover, v and w are quartic whereas θ_y and θ_z are cubic. Following the constraint strategy for e_4 and e_5, these section strains are set to be linear for this element. The resulting interpolation polynomials are given by

$$\begin{aligned} &u(\xi)=\sum_{i=1,2} L_i^{(1)}(\xi)\,u_i, && \theta_x(\xi)=\sum_{i=1,2} L_i^{(1)}(\xi)\,\theta_{xi} \\ &v(\xi)=\sum_{k=1,q,r,s,2} L_k^{(4)}(\xi)\,v_k, && w(\xi)=\sum_{k=1,q,r,s,2} L_k^{(4)}(\xi)\,w_k \\ &\theta_y(\xi)=\sum_{i=1,2} L_i^{(1)}(\xi)\,\theta_{yi}+\sum_{k=1,q,r,s,2} \overline{N}_k^{(3)}(\xi)\,w_k, && \theta_z(\xi)=\sum_{i=1,2} L_i^{(1)}(\xi)\,\theta_{zi}-\sum_{k=1,q,r,s,2} \overline{N}_k^{(3)}(\xi)\,v_k \end{aligned} \tag{23}$$

where $\overline{N}_k^{(3)}(\xi)$ $(k=1,q,r,s,2)$ are cubic polynomials that satisfy the conditions

$$e_4 = linear, \quad e_5 = linear \tag{24}$$

For the detailed expressions of the $\overline{N}_k^{(3)}(\xi)$ polynomials, refer to Appendix A. The interior dof's (v_q, v_r, v_s, w_q, w_r, and w_s, refer to Eqs. (23)) are condensed out at the element level, leading again to a twelve dof's inverse element as in Eq. (19).

4 Input data from surface strain measurements

A key step in the iFEM formulation is to evaluate the section strains due to experimentally measured surface strains. In this section, the relationships between the measured surface strains and the six section strains, e_i, are established. Also discussed are the strain gauge positions along the frame axis and their angular orientations that enable the complete description of the experimental section strains. For illustration, the present analysis is restricted to frame members with circular cross-sections; the adopted cylindrical coordinate system (θ, x, r) is shown in Figure 5.

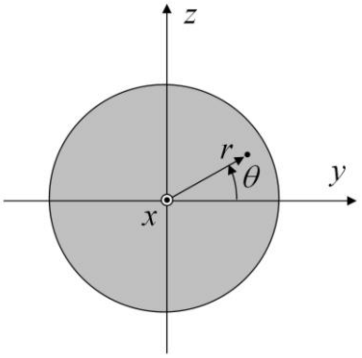

Figure 5: Orthogonal and cylindrical coordinate systems.

4.1 Section strains derived from linear strain gauge measurements

Taking the usual assumption of negligible σ_y and σ_z, then σ_x and $\tau_{x\theta}$ are the only non-zero stress components acting on the external surface $r = R_{ext}$ (Figure 6(a)). The corresponding strain state, represented in Figure 6(b), is

$$\varepsilon_x = \frac{\sigma_x}{E}, \quad \varepsilon_\theta = -\frac{\nu}{E}\sigma_x = -\nu\varepsilon_x, \quad \gamma_{x\theta} = \frac{\tau_{x\theta}}{G} \tag{25}$$

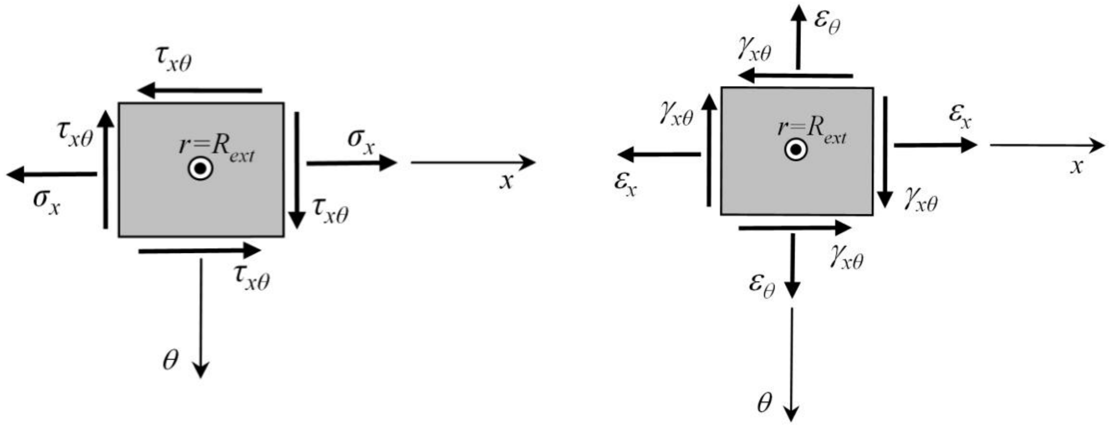

(a) Stress state. (b) Strain state.

Figure 6: Stress and strain states on the frame external surface (r=R_{ext}) in the cylindrical coordinate system.

Consider a linear strain gauge placed on the external surface at $x = x_i$, at a particular θ and with an angle β with respect to the beam axis (Figure 7); $\left(x_1^*, x_2^*, x_3^*\right)$ is a local Cartesian coordinate system having its origin on the frame external surface, the x_2^*-axis along the strain gauge measurement axis (ε_2^*), the x_1^*-axis on the frame surface and the x_3^*-axis normal to the frame surface and coincident with r-axis.

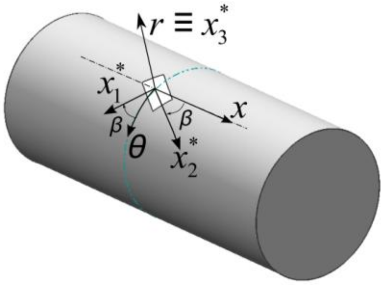

Figure 7: Location and coordinate system of a linear strain gauge placed on the frame external surface.

Using appropriate strain-tensor transformations from the $\left(\theta, x, r\right)$ to $\left(x_1^*, x_2^*, x_3^*\right)$ coordinates [27], the relationship between the measured strain ε_2^* and the strain tensor components in Eqs. (25) becomes

$$\varepsilon_2^* = \varepsilon_x \cos^2\beta + \varepsilon_\theta \sin^2\beta + \gamma_{x\theta}\cos\beta\sin\beta \tag{26}$$

or, using the second of Eqs. (25),

$$\varepsilon_2^* = \varepsilon_x \left(\cos^2 \beta - \nu \sin^2 \beta \right) + \gamma_{x\theta} \cos \beta \sin \beta \tag{27}$$

Substituting $r = R_{ext}$ in Eqs. (3), yields

$$\begin{aligned} \varepsilon_x &= e_1 + e_2 R_{ext} \sin \theta + e_3 R_{ext} \cos \theta \\ \gamma_{x\theta} &= e_4 \cos \theta - e_5 \sin \theta + e_6 R_{ext} \end{aligned} \tag{28}$$

Substituting Eq. (28) into Eq. (27) results in the relation between the measured strain ε_2^* and the six section strains at $x = x_i$

$$\begin{aligned} \varepsilon_2^* \left(x_i, \theta, \beta \right) = e_1 & \left(x_i \right) \left(c_\beta^2 - \nu s_\beta^2 \right) \\ & + e_2 \left(x_i \right) \left(c_\beta^2 - \nu s_\beta^2 \right) s_\theta R_{ext} \\ & + e_3 \left(x_i \right) \left(c_\beta^2 - \nu s_\beta^2 \right) c_\theta R_{ext} \\ & + e_4 \left(x_i \right) c_\beta s_\beta c_\theta \\ & - e_5 \left(x_i \right) c_\beta s_\beta s_\theta \\ & + e_6 \left(x_i \right) c_\beta s_\beta R_{ext} \end{aligned} \tag{29}$$

where $c_\theta \equiv \cos \theta$, $s_\theta \equiv \sin \theta$, $c_\beta \equiv \cos \beta$, and $s_\beta \equiv \sin \beta$.

4.2 Strain gauge distributions

The iFEM formulation minimizes, in the least-squares sense, Eq. (8), where $\mathbf{e}^{\boldsymbol{\varepsilon}}$ are the section strains computed from the measured strains. Thus, an important question arises what constitutes the minimum number of strain measurements.

For the 0th-order element, e_1, e_4, e_5 and e_6 are constant, whereas e_2 and e_3 are linear with respect to the axial coordinate, *x*; these section strains necessitate eight strain measurements. Similarly, for the 1st-order element, e_1 and e_6 are constant, e_4 and e_5 are linear, and e_2 and e_3 are quadratic, thus requiring twelve strain measurements.

A further reduction of strain measurements is possible if one invokes Eqs. (7). Substituting Eqs. (6) into Eqs. (7) results in

$$D_y e_{2,x} = G_z e_4, \quad D_z e_{3,x} = G_y e_5 \tag{30}$$

For the 0th-order element, Eqs. (30) give rise to two constraints equations, thus reducing the minimum number of strain measurements to six; whereas, for the 1st-order element, Eqs. (30) give rise to four constraint equations, thus reducing the minimum number of strain measurements to eight. It is worth noting that this procedure should be viewed as a convenient means of reducing the required number of strain gauges by solving for e_4 and e_5 analytically rather than measuring these quantities experimentally.

Since the strain gauges can be placed anywhere along the beam surface, the distributions considered in this study are summarized in Table 1 (also refer to Figures 8 and 9). To refer to a specific combination of the element type and strain gauge configuration, a compact notation, #-#E, is used; where the first position, #, refers to the element order (0 or 1), the second position, #, indicates the number of strain gauges per element (6 or 8), and the letter "E" indicates that Eqs. (30) have been used in the formulation. The strain gauges are placed at different positions $x = (L^e/3,\ L^e/2,\ 2L^e/3)$ along the element. The strain gauge angular orientations (θ, β) are also allowed to be different; for example, $(\theta, \beta) = (-2\pi/3,\ \pi/4)$ indicates that the strain gauge is placed at the circumferential angle $\theta=-2\pi/3$ and is oriented with an angle $\beta=\pi/4$ with respect to the frame x-axis (Figure 7).

Table 1: Strain gauge distributions x, (θ, β) corresponding to the 0th– and 1st –order elements.

Element-strain gauge notation	Orientation (θ, β) of strain gauges at $x=L^e/3$	Orientation (θ, β) of strain gauges at $x=L^e/2$	Orientation (θ, β) of strain gauges at $x=2L^e/3$
0-6E	-	$(-2\pi/3,0)$, $(-2\pi/3,\pi/4)$, $(0,0)$, $(0,\pi/4)$, $(2\pi/3,0)$, $(2\pi/3,\pi/4)$	-
1-8E	$(-2\pi/3,\pi/4)$	$(-2\pi/3,0)$, $(-2\pi/3,\pi/4)$, $(0,0)$, $(0,\pi/4)$, $(2\pi/3,0)$, $(2\pi/3,\pi/4)$	$(2\pi/3,\pi/4)$

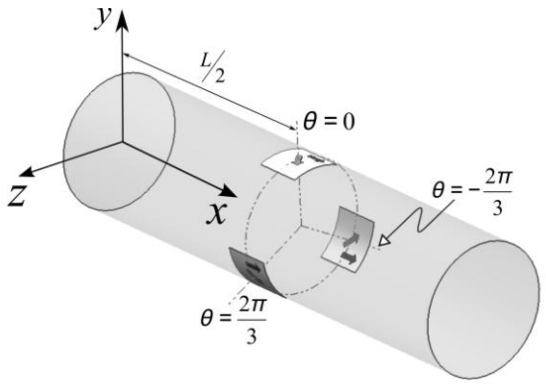

Figure 8: 0-6E strain gauge distribution.

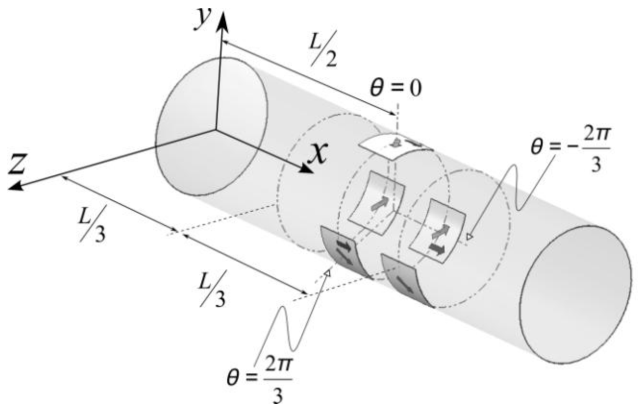

Figure 9: 1-8E strain gauge distribution.

5 Numerical results

A simple cantilevered beam subjected to dynamic loading is analyzed to assess the accuracy of the inverse finite element method. The beam is made of an aluminum alloy (E=73,000 MPa, ν=0.3, and ρ=2557 Kg/m^3) and has a thin-walled circular cross-section with the average radius R=39 mm, wall thickness s=2 mm, and length L=800 mm. The beam is fully clamped on one end and subjected at the other end to a harmonic vertical force $F_z(t)$ (where t denotes time) acting in the z-direction at frequency f_0, i.e.,

$$F_z(t) = F_{z0} \sin\left(2\pi f_0 t\right) \tag{31}$$

where F_{z0} is the force amplitude (F_{z0}=10^3 N.) To simulate the experimental-strain measurements and to assess the accuracy of the inverse method, high-fidelity direct FE analyses are performed using QUAD4 shell elements in MSC/NASTRAN. The model consists of 114 elements along the cross-sectional circumference and 360 elements along the beam axis, for a total of 41,040 elements and 41,156 nodes. The tip force is applied at the cross-sectional center at a node which is connected to all other nodes within the cross-section by means of multi-point constraints (or MPC's) [28].

The dynamic response of the beam is calculated using a modal transient analysis in MSC/NASTRAN and keeping the modes up to 5,000 Hz, with the inclusion of viscous damping of magnitude 5% with respect to the critical value at each frequency. In the frequency range from 0 to 5,000 Hz, 51 modes are present: these include the first lowest flexural beam modes, 1F-5F, appearing twice due to the cross-section symmetry, and the first membrane mode (1M). Table 2 summarizes the order of the global modes, their type, and corresponding frequency value f; the first three flexural mode shapes are shown in Figures 10-12. The other modes in this frequency range are associated with shell modes describing cross-sectional distortion and are neither shown nor tabulated.

Table 2: Global modes of the cantilevered beam in the frequency range of 0-5,000 Hz. (F-type modes are flexural; M-type modes are membrane.)

Mode order	1st and 2nd modes	3rd and 4th modes	12th mode	13th and 14th modes	30th and 31st modes	40th and 41st modes
Mode type	1F	2F	1M	3F	4F	5F
f frequency [Hz]	126.8	729.5	1,670	1,835	3,187	4,671

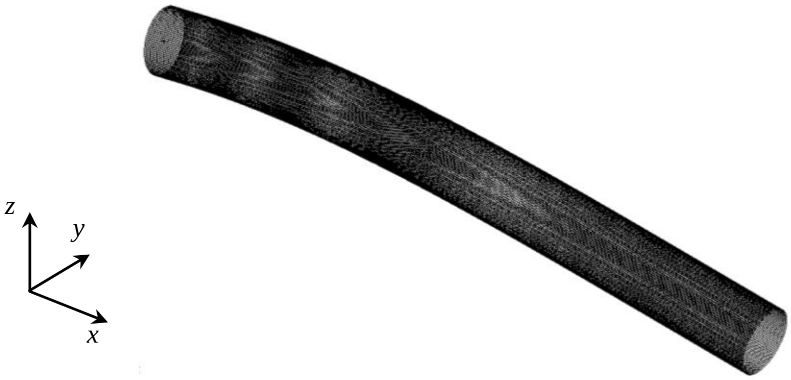

Figure 10: 1st flexural mode (1F, f = 126.8 Hz).

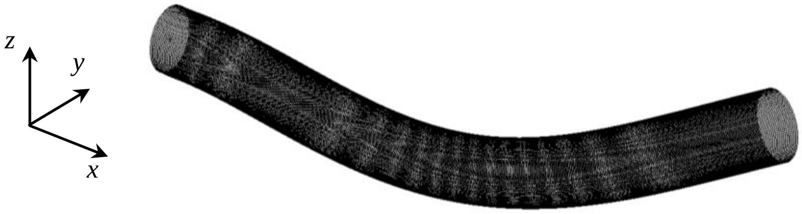

Figure 11: 2nd flexural mode (2F, f =729.5 Hz).

Figure 12: 3rd flexural mode (3F, f =1,835 Hz).

To investigate the accuracy of the iFEM modeling for dynamic applications in both low- and high-frequency regimes, three different values of the applied-force frequency f_0 have been considered, namely: f_0=60 Hz (about half of the fundamental frequency), f_0=450 Hz (halfway between the 1F and 2F modes), and f_0=1,400 Hz (halfway between the 2F and 3F modes). Figures 13-15 compare the tip-deflection time histories, $w_{max}(t)$, calculated by means of the high-fidelity FEM shell model using MSC/NASTRAN and the corresponding iFEM frame-element models. The tip deflection of the NASTRAN model corresponds to the cross-sectional center, and is computed at a node which is connected to all other nodes within the cross-section by means of MPC's. The present iFEM models used the strain-gauge distributions in Table 1 and the uniform weight coefficients $w_k^0 = 1 \quad (k = 1,...,6)$ in Eq. (10); the strain values were taken from the nodes (at the specific locations in Table 1) of the NASTRAN model. It is noted that slightly more accurate strain values reside at the element Gauss points. However, considering the high fidelity of the reference FEM model, the "measured" strains taken at the nodes are quite satisfactory.

For the low-frequency loading of f_0=60 Hz, a single 0th-order inverse element gives accurate results, with a maximum error in the tip deflection of 2.3% (Figure 13). At this excitation frequency, when

$t \geq 0.1$, viscous damping has reduced the structural vibrations to a steady state response, proceeding at a constant amplitude and the same frequency as the forcing function. When the excitation frequency of the forcing function is increased, the response has a longer transient region, which is manifested by interactions between the natural modes of vibration and that due to the applied dynamic loading. To model the transient response at higher frequencies, finer discretizations are required. Thus, for f_0 = 450 Hz, a two-element, 1st-order model yields a 1.1% error in the maximum deflection (Figure 14). At the f_0=1,400 Hz frequency, a three-element iFEM discretization using the 1st-order element results in the maximum deflection error of 2.0% (Figure 15). These results clearly demonstrate that the methodology is highly efficient, requiring only few inverse elements and strain gauge measurements, and is applicable not only for the steady state portion of the response but also for the transient regime at high frequencies.

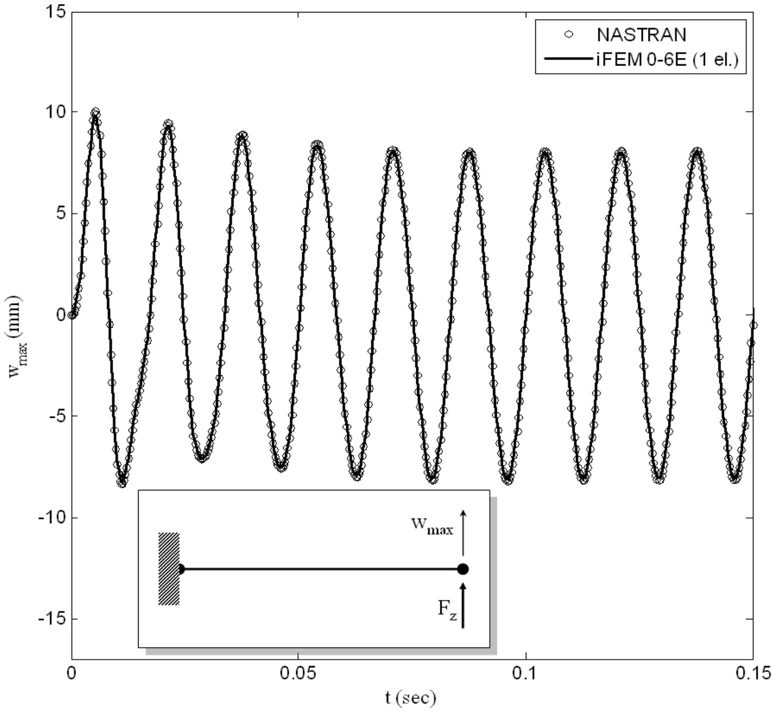

Figure 13: Tip deflection w_{max} of the beam loaded by a transverse concentrated force F_z at f_0=60 Hz.

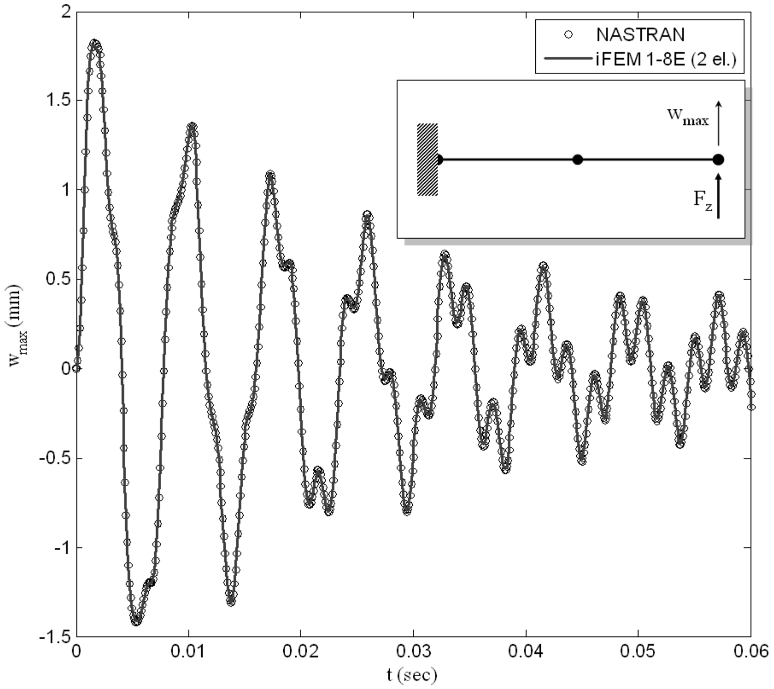

Figure 14: Tip deflection w_{max} of the beam loaded by a transverse concentrated force F_z at f_0=450 Hz.

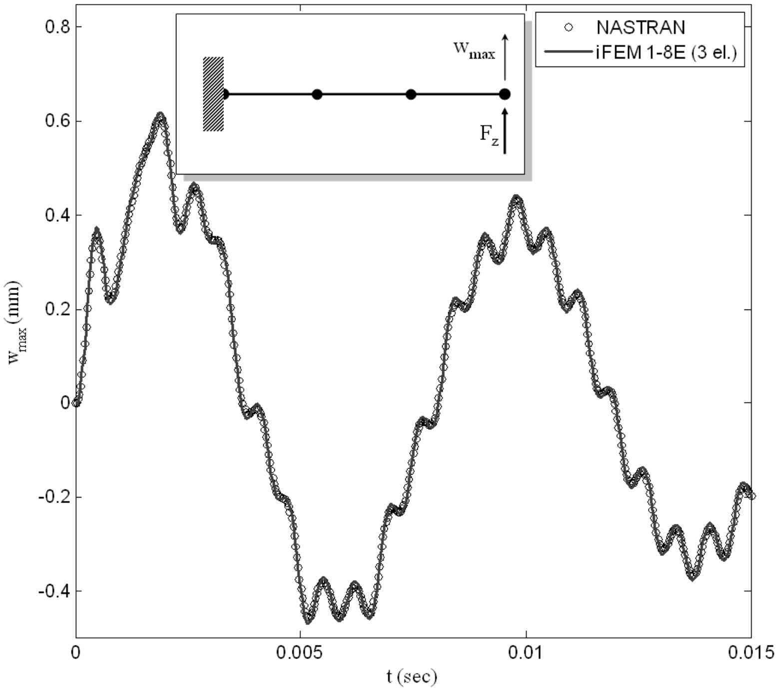

Figure 15: Tip deflection w_{max} of the beam loaded by a transverse concentrated force F_z at f_0=1,400 Hz.

6 Conclusions

In search of a suitable computational method for use in Structural Health Monitoring (SHM) systems, an inverse Finite Element Method (iFEM) has been formulated to perform the displacement-reconstruction analysis (shape-sensing) of three-dimensional frame structures undergoing static and dynamic deformations. The methodology uses a least-squares variational principle, which is discretized by C0-continuous displacement-based inverse frame elements. Linear strain-displacement relations and their components, known as section strains, are based on the Timoshenko (first-order) shear deformation theory that includes the deformations due to stretching, torsion, bending, and transverse shear. The variational statement enforces experimentally measured strains to be least-square compatible with those interpolated within the inverse frame elements. The implementation of this least-square compatibility is accomplished using the individual section strains.

Two inverse frame elements, each having two nodes and twelve dof's, have been developed. The 0th-order element has a constant shear-section strain along the element length, whereas the 1st-order element has a linear shear section strain. The element shape functions are based on interdependent interpolations that ensure locking-free bending of slender frame members. The element interpolation order is linked to the definition of the number and orientation of the uniaxial strain gauges that are necessary for the analysis. Two simple and effective strain gauge distributions have been selected and used in the numerical examples.

The present shape-sensing capability has been demonstrated on a thin-walled, circular cross-section cantilevered beam subjected to harmonic excitations in the presence of structural damping. To provide the *simulated* strain-gauge measurements, as well as the reference displacements, a high-fidelity shell finite element model was developed using the MSC/NASTRAN commercial code. Low- and high-frequency dynamic beam motions were analyzed and time history of the tip deflection examined, comparing several iFEM discretizations and strain-gauge schemes. The iFEM shape-sensing analysis, which is based only on the strain-displacement relations and the measured strain data (without any reliance on the material, inertial, or damping properties of the structure), has been shown to be highly effective and efficient in predicting the dynamic structural response of a damped beam. Accurate predictions of both the steady-state and transient response required only few elements and strain-gauge measurements, where the higher-frequency excitations necessitated somewhat higher fidelity of the iFEM models.

Although beyond the scope of the present effort, additional studies need to be performed, including: (a) shape-sensing analysis of spatial frame structures using the strains measured in a laboratory, and (b) studies of the strain-gauge distributions that provide optimal (or nearly optimal) solutions.

References

[1] A. Tessler, J.L. Spangler, A least-squares variational method for full-field reconstruction of elastic deformations in shear-deformable plates and shells, *Computer Methods in Applied Mechanics and Engineering*, **94**, 327–339, 2005.

[2] A.M. Maniatty, N.J. Zabaras, K. Stelson, Finite element analysis of some inverse elasticity problems, Journal of Engineering Mechanics, 115, 1303–1317, 1989.

[3] D.S. Schnur, N. Zabaras, Finite element solution of two-dimensional inverse elastic problems using spatial smoothing, International Journal for Numerical Methods in Engineering, 30, 57–75, 1990.

[4] A.M. Maniatty, N.J. Zabaras, Investigation of regularization parameters and error estimating in inverse elasticity problems, International Journal for Numerical Methods in Engineering, 37, 1039–1052, 1994.

[5] P.L. Liu, H.T. Lin, Direct identification of non-uniform beams using static strains, International Journal of Solids and Structures, 33, 2775–2787, 1996.

[6] M.A. Davis, A.D. Kersey, J. Sirkis, E.J. Friebele, Shape and vibration mode sensing using a fiber optic Bragg grating array, Smart Materials and Structures, 5, 759–765, 1996.

[7] L.H. Kang, D.K. Kim, J.H. Han, Estimation of dynamic structural displacements using fiber Bragg grating strain sensors, Journal of Sound and Vibration, 305, 534–542, 2007.

[8] N.S. Kim, N.S. Cho, Estimating deflection of a simple beam model using fiber optic Bragg-grating sensors, Experimental Mechanics, 44, 433–439, 2004.

[9] W.L. Ko, W.L. Richards, V.T. Fleischer, Applications of the Ko displacement theory to the deformed shape predictions of the doubly-tapered Ikhana wing, NASA/TP-2009-214652, October 2009.

[10] P.B. Bogert, E.D. Haugse, R.E. Gehrki, Structural shape identification from experimental strains using a modal transformation technique, 44th AIAA/ASME/ASCE/AHS Structures, Structural Dynamics and Materials Conference, Norfolk, Virginia, 2003.

[11] R.T. Jones, D.G. Bellemore, T.A. Berkoff, J.S. Sirkis, M.A. Davis, M.A. Putnam, E.J. Friebele, A.D. Kersey, Determination of cantilever plate shapes using wavelength division multiplexed fiber Bragg grating sensors and a least-squares strain-fitting algorithm, Smart Materials and Structures, 7, 178–188, 1998.

[12] S. Shkarayev, R. Krashantisa, A. Tessler, An inverse interpolation method utilizing in-flight strain measurements for determining loads and structural response of aerospace vehicles, 3rd International Workshop on Structural Health Monitoring, Stanford, California, 2001.

[13] S. Shkarayev, A. Raman, A. Tessler, Computational and experimental validation enabling a viable in-flight structural health monitoring technology, 1st European Workshop on Structural Health Monitoring, Cachan, Paris, France, 2002.

[14] P. Mainçon, Inverse FEM I: Load and response estimates from measurements, 2nd International Conference on Structural Engineering, Mechanics and Computation, Cape Town, South Africa, 2004.

[15] P. Mainçon, Inverse FEM II: Dynamic and non-linear problems, 2nd International Conference on Structural Engineering, Mechanics and Computation, Cape Town, South Africa, 2004.

[16] A.J. Maree, P. Mainçon, Inverse FEM III: Influence of measurement data availability, 2nd International Conference on Structural Engineering, Mechanics and Computation, Cape Town, South Africa, 2004.

[17] Barnardo, P. Mainçon, Inverse FEM IV: Influence of modelling error, 2nd International Conference on Structural Engineering, Mechanics and Computation, Cape Town, South Africa, 2004.

[18] M. Nishio, T. Mizutani, N. Takeda, Structural shape reconstruction with consideration of the reliability of distributed strain data from a Brillouin-scattering-based optical fiber sensor, Smart Materials and Structures, 19, 1-14, 2010.

[19] A. Tessler, J.L. Spangler, A variational principal for reconstruction of elastic deformation of shear deformable plates and shells, NASA TM-2003-212445, August 2003.

[20] A. Tessler, J.L. Spangler, Inverse FEM for full-field reconstruction of elastic deformations in shear deformable plates and shells, 2nd European Workshop on Structural Health Monitoring, Munich, Germany, 2004.

[21] S.L. Vazquez, A. Tessler, C.C. Quach, E.G. Cooper, J. Parks, J.L. Spangler, Structural health monitoring using high-density fiber optic strain sensor and inverse finite element methods, NASA TM-2005-213761, May 2005.

[22] C.C. Quach, S.L. Vazquez, A. Tessler, J.P. Moore, E.G. Cooper, J.L. Spangler, Structural anomaly detection using fiber optic sensors and inverse finite element method, AIAA Guidance, Navigation, and Control Conference and Exhibit, San Francisco, California, 2005.

[23] P. Cerracchio, M. Gherlone, M. Mattone, M. Di Sciuva, A. Tessler, Shape sensing of three-dimensional frame structures using the inverse finite element method, 5th European Workshop on Structural Health Monitoring, Sorrento, Italy, 2010.

[24] M. Gherlone, P. Cerracchio, M. Mattone, M. Di Sciuva, A. Tessler, Dynamic shape reconstruction of three-dimensional frame structures using the inverse finite element method, 3rd ECCOMAS Thematic Conference on Computational Methods in Structural Dynamics and Earthquake Engineering, Corfù, Greece, 2011.

[25] S.P. Timoshenko, On the correction for shear of differential equations for transverse vibrations of prismatic bars, Philosophical Magazine, 41, 744–746, 1921.

[26] A. Tessler, S.B. Dong, On a hierarchy of conforming Timoshenko beam elements, Computers & Structures, 14, 335–344, 1981.

[27] A.I. Lurie, Theory of Elasticity, Springer-Verlag Berlin Heidelberg, New York, 2005.

[28] MSC/MD-NASTRAN, Reference Guide, Version 2006.0, MSC Software Corporation, Santa Ana, CA.

Appendix A

The 1st, 2nd, and 4th-degree Lagrange shape functions are given as

- 1st degree

$$\left[L_1^{(1)}, L_2^{(1)}\right] \equiv \frac{1}{2}\left[\left(1-\xi\right), \left(1+\xi\right)\right] \tag{A1}$$

- 2nd degree

$$\left[L_1^{(2)}, L_r^{(2)}, L_2^{(2)}\right] \equiv \frac{1}{2}\left[\xi\left(\xi-1\right), 2\left(1-\xi^2\right), \xi\left(\xi+1\right)\right] \tag{A2}$$

- 4th degree

$$\begin{gathered}\left[L_1^{(4)}, L_2^{(4)}\right] \equiv \frac{1}{6}\xi\left(4\xi^2-1\right)\left[\left(\xi-1\right), \left(\xi+1\right)\right] \\ \left[L_q^{(4)}, L_r^{(4)}, L_s^{(4)}\right] \equiv \frac{1}{3}\left(1-\xi^2\right)\left[4\xi\left(2\xi-1\right), 3\left(1-4\xi^2\right), 4\xi\left(2\xi+1\right)\right]\end{gathered} \tag{A3}$$

where $\xi \equiv 2x/L^e - 1 \in \left[-1,1\right]$ is a non-dimensional axial coordinate; $x \in \left[0, L^e\right]$ and L^e denotes the element length. The subscripts 1 and 2 represent the end nodes, whereas *q*, *r*, and *s* denote the uniformly spaced interior nodes.

The 3rd –degree shape functions, $N_j^{(3)}\left(\xi\right)$, of the 0th-order element have the form

$$\left[N_1^{(3)}, N_r^{(3)}, N_2^{(3)}\right] \equiv \frac{L^e}{24}\left(1-\xi^2\right)\left[\left(2\xi-3\right), -4\xi, \left(2\xi+3\right)\right] \tag{A4}$$

whereas the cubic $\overline{N}_k^{(3)}\left(\xi\right)$ shape functions of the 1st-order element are

$$\left[\overline{N}_1^{(3)}, \overline{N}_q^{(3)}, \overline{N}_r^{(3)}, \overline{N}_s^{(3)}, \overline{N}_2^{(3)}\right] \equiv \frac{4}{3L^e}\left(1-\xi^2\right)\left[\left(4\xi-3\right), -2\left(8\xi-3\right), 24\xi, -2\left(8\xi+3\right), \left(4\xi+3\right)\right] \tag{A5}$$

Appendix B

The matrix $\mathbf{B}$ relating the section strains to the element dof's may be written as follows

$$\mathbf{B}\left(\xi\right) = \begin{bmatrix} \mathbf{B}_1 \\ \mathbf{B}_2 \\ \mathbf{B}_3 \\ \mathbf{B}_4 \\ \mathbf{B}_5 \\ \mathbf{B}_6 \end{bmatrix} = \begin{bmatrix} \mathbf{B}_{11} & \mathbf{0} & \mathbf{B}_{12} \\ \mathbf{B}_{21} & \mathbf{B}_{2c} & \mathbf{B}_{22} \\ \mathbf{B}_{31} & \mathbf{B}_{3c} & \mathbf{B}_{32} \\ \mathbf{B}_{41} & \mathbf{B}_{4c} & \mathbf{B}_{42} \\ \mathbf{B}_{51} & \mathbf{B}_{5c} & \mathbf{B}_{52} \\ \mathbf{B}_{61} & \mathbf{0} & \mathbf{B}_{62} \end{bmatrix} \tag{B1}$$

For a 0th-order element, $\mathbf{0}$ is a 1x2 null matrix and the other sub-matrices are defined below

$$\left.\begin{aligned}
\mathbf{B}_{1i} &\equiv \frac{2}{L^e}\begin{bmatrix} L_{i,\xi}^{(1)} & 0 & 0 & 0 & 0 & 0 \end{bmatrix} \\
\mathbf{B}_{2i} &\equiv \frac{2}{L^e}\begin{bmatrix} 0 & 0 & 0 & 0 & L_{i,\xi}^{(2)} & 0 \end{bmatrix} \\
\mathbf{B}_{3i} &\equiv \frac{2}{L^e}\begin{bmatrix} 0 & 0 & 0 & 0 & 0 & -L_{i,\xi}^{(2)} \end{bmatrix} \\
\mathbf{B}_{4i} &\equiv \frac{2}{L^e}\begin{bmatrix} 0 & 0 & L_{i,\xi}^{(1)} & 0 & \left(N_{i,\xi}^{(3)} + \dfrac{L^e L_i^{(2)}}{2}\right) & 0 \end{bmatrix} \\
\mathbf{B}_{5i} &\equiv \frac{2}{L^e}\begin{bmatrix} 0 & L_{i,\xi}^{(1)} & 0 & 0 & 0 & -\left(N_{i,\xi}^{(3)} + \dfrac{L^e L_i^{(2)}}{2}\right) \end{bmatrix} \\
\mathbf{B}_{6i} &\equiv \frac{2}{L^e}\begin{bmatrix} 0 & 0 & 0 & L_{i,\xi}^{(1)} & 0 & 0 \end{bmatrix}
\end{aligned}\right\} \quad (i=1,2) \tag{B2}$$

$$
\begin{aligned}
\mathbf{B}_{2c} &\equiv \frac{2}{L^e}\begin{bmatrix} L^{(2)}_{r,\xi} & 0 \end{bmatrix} \\
\mathbf{B}_{3c} &\equiv \frac{2}{L^e}\begin{bmatrix} 0 & -L^{(2)}_{r,\xi} \end{bmatrix} \\
\mathbf{B}_{4c} &\equiv \frac{2}{L^e}\begin{bmatrix} \left(N^{(3)}_{r,\xi} + \dfrac{L^e L^{(2)}_{r}}{2} \right) & 0 \end{bmatrix} \\
\mathbf{B}_{5c} &\equiv \frac{2}{L^e}\begin{bmatrix} 0 & -\left(N^{(3)}_{r,\xi} + \dfrac{L^e L^{(2)}_{r}}{2} \right) \end{bmatrix}
\end{aligned}
\tag{B3}
$$

For a 1st-order element, $\mathbf{0}$ is a 1x6 null matrix and the other sub-matrices are defined below

$$
\left.
\begin{aligned}
\mathbf{B}_{1i} &\equiv \frac{2}{L^e}\begin{bmatrix} L^{(1)}_{i,\xi} & 0 & 0 & 0 & 0 & 0 \end{bmatrix} \\
\mathbf{B}_{2i} &\equiv \frac{2}{L^e}\begin{bmatrix} 0 & 0 & \overline{N}^{(3)}_{i,\xi} & 0 & L^{(2)}_{i,\xi} & 0 \end{bmatrix} \\
\mathbf{B}_{3i} &\equiv \frac{2}{L^e}\begin{bmatrix} 0 & \overline{N}^{(3)}_{i,\xi} & 0 & 0 & 0 & -L^{(2)}_{i,\xi} \end{bmatrix} \\
\mathbf{B}_{4i} &\equiv \frac{2}{L^e}\begin{bmatrix} 0 & 0 & \left(L^{(4)}_{i,\xi} + \dfrac{L^e \overline{N}^{(3)}_{i}}{2} \right) & 0 & \dfrac{L^e L^{(2)}_{i}}{2} & 0 \end{bmatrix} \\
\mathbf{B}_{5i} &\equiv \frac{2}{L^e}\begin{bmatrix} 0 & \left(L^{(4)}_{i,\xi} + \dfrac{L^e \overline{N}^{(3)}_{i}}{2} \right) & 0 & 0 & 0 & -\dfrac{L^e L^{(2)}_{i}}{2} \end{bmatrix} \\
\mathbf{B}_{6i} &\equiv \frac{2}{L^e}\begin{bmatrix} 0 & 0 & 0 & L^{(1)}_{i,\xi} & 0 & 0 \end{bmatrix}
\end{aligned}
\right\} \quad (i = 1, 2)
\tag{B4}
$$

$$
\begin{aligned}
\mathbf{B}_{2c} &\equiv \frac{2}{L^e}\begin{bmatrix} 0 & \overline{N}^{(3)}_{q,\xi} & 0 & \overline{N}^{(3)}_{r,\xi} & 0 & \overline{N}^{(3)}_{s,\xi} \end{bmatrix} \\
\mathbf{B}_{3c} &\equiv \frac{2}{L^e}\begin{bmatrix} \overline{N}^{(3)}_{q,\xi} & 0 & \overline{N}^{(3)}_{r,\xi} & 0 & \overline{N}^{(3)}_{s,\xi} & 0 \end{bmatrix} \\
\mathbf{B}_{4c} &\equiv \frac{2}{L^e}\begin{bmatrix} 0 & \left(L^{(4)}_{q,\xi} + \dfrac{L^e \overline{N}^{(3)}_{q}}{2} \right) & 0 & \left(L^{(4)}_{r,\xi} + \dfrac{L^e \overline{N}^{(3)}_{r}}{2} \right) & 0 & \left(L^{(4)}_{s,\xi} + \dfrac{L^e \overline{N}^{(3)}_{s}}{2} \right) \end{bmatrix} \\
\mathbf{B}_{5c} &\equiv \frac{2}{L^e}\begin{bmatrix} \left(L^{(4)}_{q,\xi} + \dfrac{L^e \overline{N}^{(3)}_{q}}{2} \right) & 0 & \left(L^{(4)}_{r,\xi} + \dfrac{L^e \overline{N}^{(3)}_{r}}{2} \right) & 0 & \left(L^{(4)}_{s,\xi} + \dfrac{L^e \overline{N}^{(3)}_{s}}{2} \right) & 0 \end{bmatrix}
\end{aligned}
\tag{B5}
$$

REPORT DOCUMENTATION PAGE

Form Approved
OMB No. 0704-0188

1. REPORT DATE *(DD-MM-YYYY)*
01- 12 - 2011

2. REPORT TYPE
Technical Publication

3. DATES COVERED *(From - To)*

4. TITLE AND SUBTITLE
Dynamic Shape Reconstruction of Three-Dimensional Frame Structures Using the Inverse Finite Element Method

5a. CONTRACT NUMBER

5b. GRANT NUMBER

5c. PROGRAM ELEMENT NUMBER

6. AUTHOR(S)
Gherlone, Marco; Cerrachio, Priscilla; Mattone, Massimiliano; Di Sciuva, Marco; Tessler, Alexander

5d. PROJECT NUMBER

5e. TASK NUMBER

5f. WORK UNIT NUMBER
284848.02.03.07.01

7. PERFORMING ORGANIZATION NAME(S) AND ADDRESS(ES)
NASA Langley Research Center
Hampton, VA 23681-2199

8. PERFORMING ORGANIZATION REPORT NUMBER
L-20096

9. SPONSORING/MONITORING AGENCY NAME(S) AND ADDRESS(ES)
National Aeronautics and Space Administration
Washington, DC 20546-0001

10. SPONSOR/MONITOR'S ACRONYM(S)
NASA

11. SPONSOR/MONITOR'S REPORT NUMBER(S)
NASA/TP-2011-217315

12. DISTRIBUTION/AVAILABILITY STATEMENT
Unclassified Unlimited
Subject Category 39
Availability: NASA CASI (443) 757-5802

13. SUPPLEMENTARY NOTES

14. ABSTRACT

A robust and efficient computational method for reconstructing the three-dimensional displacement field of truss, beam, and frame structures, using measured surface-strain data, is presented. Known as “shape sensing”, this inverse problem has important implications for real-time actuation and control of smart structures, and for monitoring of structural integrity. The present formulation, based on the inverse Finite Element Method (iFEM), uses a least-squares variational principle involving strain measures of Timoshenko theory for stretching, torsion, bending, and transverse shear. Two inverse-frame finite elements are derived using interdependent interpolations whose interior degrees-of-freedom are condensed out at the element level. In addition, relationships between the order of kinematic-element interpolations and the number of required strain gauges are established. As an example problem, a thin-walled, circular cross-section cantilevered beam subjected to harmonic excitations in the presence of structural damping is modeled using iFEM; where, to simulate strain-gauge values and to provide reference displacements, a high-fidelity MSC/NASTRAN shell finite element model is used. Examples of low and high-frequency dynamic motion are analyzed and the solution accuracy examined with respect to various levels of discretization and the number of strain gauges.

15. SUBJECT TERMS

Frame finite element; Inverse Finite Element Method; Structural Health Monitoring; Timoshenko beam theory; Variational principle

16. SECURITY CLASSIFICATION OF:			17. LIMITATION OF ABSTRACT	18. NUMBER OF PAGES	19a. NAME OF RESPONSIBLE PERSON
a. REPORT	b. ABSTRACT	c. THIS PAGE			STI Help Desk (email: help@sti.nasa.gov)
					19b. TELEPHONE NUMBER *(Include area code)*
U	U	U	UU	30	(443) 757-5802

Standard Form 298 (Rev. 8-98)
Prescribed by ANSI Std. Z39.18